

Event-based Human Pose Tracking by Spiking Spatiotemporal Transformer

Shihao Zou, Yuxuan Mu, Xinxin Zuo, Sen Wang, Li Cheng

Abstract—Event camera, as an emerging biologically-inspired vision sensor for capturing motion dynamics, presents new potential for 3D human pose tracking, or video-based 3D human pose estimation. However, existing works in pose tracking either require the presence of additional gray-scale images to establish a solid starting pose, or ignore the temporal dependencies all together by collapsing segments of event streams to form static event frames. Meanwhile, although the effectiveness of Artificial Neural Networks (ANNs, a.k.a. *dense deep learning*) has been showcased in many event-based tasks, the use of ANNs tends to neglect the fact that compared to the dense frame-based image sequences, the occurrence of events from an event camera is spatiotemporally much sparser. Motivated by the above mentioned issues, we present in this paper a dedicated end-to-end *sparse deep learning* approach for event-based pose tracking: 1) to our knowledge this is the first time that 3D human pose tracking is obtained from events only, thus eliminating the need of accessing to any frame-based images as part of input; 2) our approach is based entirely upon the framework of Spiking Neural Networks (SNNs), which consists of Spike-Element-Wise (SEW) ResNet and a novel Spiking Spatiotemporal Transformer; 3) a large-scale synthetic dataset is constructed that features a broad and diverse set of annotated 3D human motions, as well as longer hours of event stream data, named SynEventHPD. Empirical experiments demonstrate that, with superior performance over the state-of-the-art (SOTA) ANNs counterparts, our approach also achieves a significant computation reduction of 80% in FLOPs. Furthermore, our proposed method also outperforms SOTA SNNs in the regression task of human pose tracking. Our implementation is available at https://github.com/JimmyZou/HumanPoseTracking_SNN and dataset will be released upon paper acceptance.

Index Terms—Human Pose Tracking, Event Camera, Spiking Neural Networks

1 INTRODUCTION

As an important area of research in computer vision, visual human pose tracking has attracted increasing research attentions in recent years. While most current research efforts have been focused on RGB or depth cameras [1]–[16], event camera [17], as an emerging vision sensor, presents new opportunities in this area. As a novel and biologically-inspired vision system, event camera is considerably dissimilar to the conventional frame-based cameras. In particular, by adopting its unique asynchronous and independent address-event representation, event camera is capable of imaging high-speed motions with a very low power consumption. This innovative imaging paradigm has sparked a multitude of research efforts in the field of event-based vision, such as tracking [18]–[21], recognition [22]–[24], 3D reconstruction [25], [26], and a diverse range of applications in robotics, augmented and virtual reality, and autonomous driving [17].

Recently, data-driven approaches have shown their potential for effective pose estimation from event cameras [27]–[30]. One of the earliest approaches [27] uses Convolutional Neural Networks (CNNs) to estimate 2D human poses from event frames. EventCap [28] expands upon this by capturing fast 3D human motion based on an event stream, as well as a sequence of gray-scale images to establish initial poses over time. The most recent approach, EventHPE [29], reduces the reliance on gray-scale images by using only

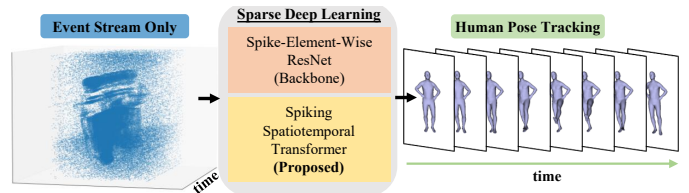


Fig. 1. **Overview of our approach.** An end-to-end sparse deep learning approach is proposed for 3D single-person pose tracking over time from event streams only. Specifically, our method incorporates SEW ResNet as its backbone, and a novel Spiking Spatiotemporal Transformer to address one-directional temporal dependency issue in SNNs.

the first gray-scale frame to extract the starting pose, then relying solely on the event stream for subsequent pose tracking. The concurrent work of [30] instead focuses on static hand pose estimation from event camera, by engaging an CNNs method. Unfortunately, existing methods either require additional gray-scale images [28], [29] which are too dense for practical efficiency, or treat the event stream as a static event frame [27], [30], thus discarding temporal dependencies that could be critical in pose tracking. As a result, the full potential of human pose tracking using only the event stream remains largely unexploited.

Meanwhile, artificial neural networks (ANNs), such as ResNet [31] and Transformer [32], have demonstrated their potential in various event-based vision tasks [19], [20], [22]–[24], [30], [33]–[38]. However, compared with dense RGB or gray-scale images, event streams are *spatiotemporally much sparser*, resulting in a growing interest in seeking ways to process events more efficiently. One promising strategy is based on the Spiking Neural Networks (SNNs). Unlike traditional ANNs, spiking neurons are employed in SNNs to imitate the event generation process, thus bypassing

- S. Zou, Y. Mu, X. Zuo, S. Wang and L. Cheng are with the Department of Electrical and Computer Engineering, University of Alberta, Edmonton, AB, Canada, T6G 2W3. (E-mail: szou2@ualberta.ca, lcheng5@ualberta.ca) Li Cheng is the corresponding author.

the unnecessary computations in inactive or non-spiking neurons. Previous efforts have shown the superiority of SNNs in classification tasks, including converting ANNs to SNNs [39]–[43], or training SNNs from scratch [24], [35], [44]–[47]. There are also attempts [21], [48] proposing a mixed framework of SNNs and ANNs to balance the efficiency and performance in event-based regression tasks. However, the challenge of conducting pose tracking solely using event signals, and exclusively engaging the SNNs architecture to fully exploit the innate sparsity in events data, remains unaddressed. This may be attributed to the following three challenges. (i) Unlike spike votes used in classification, regression is sensitive to the output values, which may result in additional quantization errors in pose prediction due to the compact spike representation in SNNs. (ii) As opposed to high-level label prediction in the static classification tasks, pose tracking requires fine-grained regression of pose over time. (iii) Spikes are typically unfolded over time, which naturally preserves only one-directional temporal dependency in SNNs. This may lead to insufficient pose information, especially when the character is not moving in the starting phase and thereby few events are observed for pose estimation.

Motivated by the above observations, our work aims to tackle a relatively new problem of tracking 3D human poses solely based on event streams from an event camera, thus completely eliminating the need for additional input dense images. As presented in Fig. 2, our approach is an end-to-end sparse deep learning approach that estimates parametric human poses over time solely from events. This model is entirely built upon SNNs, thus having the promise of being more efficient than that of the dense deep learning models (i.e. ANNs). The input event stream goes through a preprocessing step to form a sequence of event voxel grids; Spike-Element-Wise (SEW) ResNet [24] is then employed as the SNNs backbone to extract pose spike features; this is followed by our proposed Spiking Spatiotemporal Transformer that carries bi-directional fusion of the acquired pose spike features, allowing for the distribution of pose information especially to those at the early time intervals. In our spiking transformer, the attention score between binary spike vectors utilizes a normalized Hamming similarity, which, as shown in Proposition 1, amounts to the scaled dot-product similarity between the real valued vectors used by the standard transformer [32]. In the final step, 2D average pooling is applied to the spatiotemporally aggregated spike features, which is followed by a direct regression to output the parametric 3D human poses over time.

Our contributions can be summarized as follows:

- This work addresses a relatively new task of 3D human pose tracking **solely based on events** from an event camera.
- We propose an end-to-end SNN-based approach, which specifically incorporates a novel **Spiking Spatiotemporal Transformer** module to tackle the one-directional temporal dependency issue. This allows for the propagation of pose-related information to facilitate pose estimation especially for the early time steps. Extensive empirical experiments demonstrate the superior performance of our approach over exist-

ing SOTA methods, including EventCap [28], EventHPE [29] and a few ANN baselines [15], [49], [50]. Further, this is achieved by utilizing merely around 20% of the computation (in FLOPs) required by the SOTA methods. Furthermore, our proposed method also outperforms SOTA SNN baselines [24], [46], [47] in this regression task of human pose tracking.

- **A large-scale dataset, SynEventHPD**, is constructed for the task of event-based 3D human pose tracking. It consists of synthesized events data from multiple motion capture datasets (i.e. *Human3.6M* [51], *AMASS* [52], *PHSPD* [53] and *MMHPSD-Gray* [29]). Consequently, it covers a variety of motions such as juggling, moon-walking, jumping rope, vaulting and scampering, with a total size of 45.72 hours event streams – more than 10 times larger than MMHPSD [29], the largest existing event-based pose tracking dataset. The details are summarized in Tab. 1, and empirical studies have suggested the usefulness of our new dataset.

2 RELATED WORK

Here we provide a concise overview of the related efforts. More detail could be found in the supplementary file.

Human pose estimation from RGB or depth images has been a popular topic in computer vision in recent years. Prior to the deep learning era, research efforts are mainly based on random forest [1], [4] or dictionary learning [5], [6]. Benefited from the significant performance boosts brought by deep learning, recent efforts in human pose estimation either directly regress 3D pose from images [7], [8] or lift 2D pose estimation to 3D [2], [3]. This trend is further fueled by the development of SMPL [54], a parametric human shape model of low-dimensional statistical representation. HMR [9] is the first such effort in applying convolutional neural networks for human SMPL shape recovery from single images, which produces impressive results. Several recent efforts also emphasize on the exploitation of temporal information in inferring human poses and shapes from videos, including e.g. temporal constraints [14], [15], [55], dynamic cameras [16] or event signals [28], [29].

Event-based vision applications have witnessed a substantial increase in recent years. As for human pose tracking, DHP19 [27] is perhaps the first effort in engaging event camera for human 2D pose estimation using CNNs. EventCap [28] aims to capture 3D motions from both events and gray-scale images provided by an event camera. It starts with a pre-trained CNN-based 3D pose estimation module that takes a sequence of low-frequency gray-scale images as input; the estimated poses are then used as the initial state to infill the intermediate poses for high-frequency motion capture with the constraint of detected event trajectories by [18]. These methods, however, require full access to the corresponding gray-scale images as co-input. EventHPE [29] reduces this demand by the milder requirement of only a single gray-scale image of the starting pose. In doing so, a dedicated CNNs module is trained to infer optical flow by self-supervised learning, which is used alongside with the input event stream to reconstruct the 3D full-body shapes. Compared with these existing efforts [28], [29], our approach requires only the events as input, where a

novel SNN-based framework is utilized to produce better shape reconstruction results with much less computation footprint.

Event-based datasets are crucial for data-driven approaches to attain their satisfactory performance. Unfortunately, existing benchmark datasets [51], [56] are mostly based on conventional RGB or depth cameras – thus are infeasible to be directly used in event-based tasks, given the fundamental differences between event and conventional cameras. As for event-based human pose estimation, DHP19 dataset [27] is the earliest one, which however contains rather limited amount of events data that also lack pose variety. The most recent released dataset is MMPHSPD [29] built with event camera and 3 other imaging devices. Although the dataset provides more than 4.5 hours event stream and 21 different types of action, it may still lack sufficient degree of pose variety, partly due to its in-house capturing setup. In this work, we significantly augment the MMPHSPD dataset by synthesizing events data from several human motion capture benchmark datasets [29], [51]–[53] – it gives rise to a large-scale dataset, SynEventHPD, containing a rich variety of poses for the task of event-based human pose tracking. This dataset will be instrumental in further facilitating the research on event-based vision and SNNs for human pose tracking.

Training large-scale SNNs from scratch presents a significant challenge. To alleviate the non-differentiable issue of neuronal spiking function, one branch of works focus on converting trained ANNs to SNNs [39]–[43]. Typically, such ANN2SNN methods map the non-linear activation layer in a trained ANNs to a neuron spiking layer and scale the threshold or the weights accordingly. It is worth noting that only in the realm of classification tasks, excellent results have been demonstrated by the SNNs methods; in fine-grained regression tasks and specifically in human pose estimation, the SNNs performance is still inadequate. Another branch of works, on the other hand, focus on training SNNs from scratch, often by following the backpropagation through time (BPTT) framework and applying surrogate derivatives [44] to approximate the gradient of neuronal spiking function. This line of works have delivered impressive performance in classification tasks [24], [35], [44]–[47] as well as regression tasks [57]. Our proposed work can be regarded as an attempt along this direction, with its focus on the fine-grained regression task of full-body pose tracking.

Spiking Transformer has emerged very recently as a new SNNs architecture. To avoid confusion, it is important to note that the spiking transformers presented in [21], [58] are not SNN-based transformers, but rather ANN-based or mixed models. The two recent works [46], [47] are most related to our proposed spiking spatiotemporal transformer. In MA-SNN [46], multi-dimensional attention is proposed in an SNNs framework, yet this attention is instead based on real values of membrane potentials, thus in a sense violating the efficiency design of SNNs. In contrast, the spatiotemporal attention mechanism in our model is entirely based on spike tensors, which is realised by the proposed Hamming similarity score. Our work is also very different from Spikformer [47], where the scaled dot-product is directly adopted to compute the similarity score. As analysed in

Sec. 4.3, this function may not be well-defined for binary vectors.

3 PRELIMINARY

In this section, we will discuss spiking neuron model, feedforward process in SNNs, computational consumption of SNNs, and the attention mechanism in the standard transformer. Details on backpropagation can be found in the supplementary material.

Spiking neuron model commonly refers to the leaky integrate and fire (LIF) model, a fundamental unit in SNNs. A LIF neuron maintains a membrane potential $u_{[t]}$ with a leaky constant τ , which may be modified only when new spiking trains $X_{[t]}$ are received from its connected neurons in T time steps. The neuron then outputs a spike $s_{[t]}$ and reset its potential by $V_{th} - u_{rest}$, if its potential exceeds a predetermined threshold, V_{th} , where soft reset [24] is adopted in our work. The model is formulated as follows:

$$h_{[t]} = u_{[t-1]} - \frac{1}{\tau}(u_{[t-1]} - u_{rest}) + X_{[t]}, \quad (1)$$

$$s_{[t]} = \Theta(h_{[t]} - V_{th}), \quad (2)$$

$$u_{[t]} = h_{[t]} - (V_{th} - u_{rest})s_{[t]}, \quad (3)$$

where Θ is the Heaviside step function,

$$\Theta(h_{[t]} - V_{th}) = \begin{cases} 1, & \text{if } h_{[t]} - V_{th} \geq 0 \\ 0, & \text{otherwise.} \end{cases} \quad (4)$$

Feedforward in SNNs consists of multiple layers of connected spiking neurons. Assume there are $N^{(l)}$ neurons in the l -th layer, and use the vector forms of $\mathbf{u}_{[t]}^{(l)} \in \mathbb{R}^{N^{(l)}}$ and $\mathbf{s}_{[t]}^{(l)} \in \{0, 1\}^{N^{(l)}}$ to represent their respective membrane potentials and output spikes at time step t . Let $\mathbf{W}^l \in \mathbb{R}^{N^{(l)} \times N^{(l-1)}}$ denote the connecting weights between layer $l - 1$ and l , $\lambda = 1 - \frac{1}{\tau}$ be the leaky constant of LIF neuron model, and set u_{rest} to 0, feedforward in SNNs becomes

$$\mathbf{h}_{[t]}^{(l)} = \underbrace{\lambda \mathbf{u}_{[t-1]}^{(l)}}_{\text{leak}} + \underbrace{\mathbf{W}^l \mathbf{s}_{[t]}^{(l-1)}}_{\text{charge}}, \quad (5)$$

$$\mathbf{s}_{[t]}^{(l)} = \underbrace{\Theta(\mathbf{h}_{[t]}^{(l)} - V_{th})}_{\text{spike}}, \quad (6)$$

$$\mathbf{u}_{[t]}^{(l)} = \underbrace{\mathbf{h}_{[t]}^{(l)} - V_{th} \mathbf{s}_{[t]}^{(l)}}_{\text{reset}}. \quad (7)$$

Computational consumption of SNNs is often lower than ANNs, partly owing to the binary output of spiking neurons. Considering binary spikes $\mathbf{s}_{[t]}^{(l-1)}$ in layer $l - 1$ and $\mathbf{s}_{[t]}^{(l)}$ in layer l , the computations of inactive neurons ($s_{[t]} = 0$) can be skipped. Assuming the spiking rate is ρ for the layer, from Eq. (5) and (6), a linear layer plus a spiking layer in SNN requires merely $\mathcal{O}(\rho T N^{(l-1)} N^{(l)})$ FLOPs¹ for T time steps, while in ANNs, a linear layer plus a non-linear ReLU layer requires $\mathcal{O}(T N^{(l-1)} N^{(l)})$ FLOPs. Normally, ρ is around 20% in average, which means SNNs require only around 20% FLOPs of that required by ANNs.

1. FLOPs refers to the number of floating point operations.

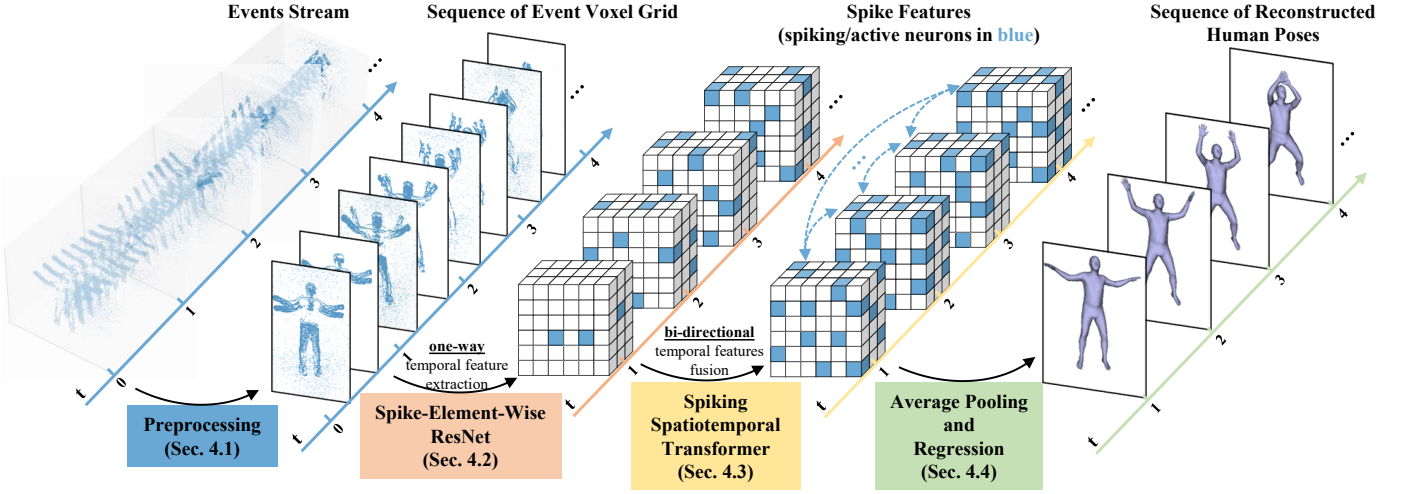


Fig. 2. **Pipeline of our sparse deep learning approach.** It contains four main sections: (i) **Preprocessing** in Sec. 4.1 converts a stream of events into a sequence of event voxel grids of the same temporal length. (ii) **SEW-ResNet** [24], introduced in Sec. 4.2, is used as backbone to extract pose spike features given the input event voxel grids. Hidden neurons in spiking (active) status are shown in blue. (iii) **A novel spiking spatiotemporal transformer** is proposed in Sec. 4.3 for the bi-directional fusion of pose spike features. The proposed spiking spatiotemporal attention allows bi-directional flow of information over time in SNNs, thus facilitating pose estimation especially for the early time steps. (iv) **Parametric human poses tracking** is presented in Sec. 4.4, where average pooling is applied to the spatiotemporally aggregated spike features before regressing the human pose and shape parameters.

Scaled dot-product attention is defined as

$$\text{Attention}(\mathbf{Q}, \mathbf{K}, \mathbf{V}) = \text{softmax}\left(\frac{\mathbf{Q}\mathbf{K}^\top}{\sqrt{d_k}}\right)\mathbf{V}, \quad (8)$$

in the standard transformer [32], where $\mathbf{Q}, \mathbf{K} \in \mathbb{R}^{N \times d_k}$ are queries and keys and $\mathbf{V} \in \mathbb{R}^{N \times d_v}$ is values, with N being the length of input sequence, d_k the dimension of a single query \mathbf{q} or key \mathbf{k} , and d_v the dimension of a single value \mathbf{v} . The scaling factor of $1/\sqrt{d_k}$ is to normalize the dot-product $\mathbf{q}\mathbf{k}^\top$ to have mean 0 and variance 1, assuming the components of \mathbf{q} and \mathbf{k} are independent variables with mean 0 and variance 1.

4 OUR APPROACH

As summarized in Fig. 2, our approach consists of four main sections. (i) Preprocessing in Sec. 4.1, is to convert an stream of event into a sequence of event voxel grids [17] with the same time interval. (ii) SEW-ResNet [24] in Sec. 4.2, is employed as the backbone to extract pose spike features from the input sequence of event voxel. (iii) Since SEW-ResNet only considers the one-directional temporal relationship, we propose a novel Spiking Spatiotemporal Transformer for the bi-directional fusion of pose spike features in Sec. 4.3, allowing for the compensation of missing pose information, especially for the early time steps. (iv) The final stage, illustrated in Sec. 4.4, is to apply average pooling to the spatiotemporally aggregated spike features and then regress the parametric poses over time. In this work, a stream of events is the sole source of input, thus eliminating the reliance on gray-scale input images as in [28] or a prior knowledge of the starting pose as in [29]. Furthermore, our model is completely built upon SNNs instead of traditional ANNs or mixed architecture.

4.1 Preprocessing

Instead of a sequence of RGB frames captured by an RGB camera, an asynchronous stream of independent event signals is assembled by an event camera as the input signals. This event stream is decomposed into a sequence of T packets of events, with each packet spanning the same

time length, $\mathcal{E} = \{\mathcal{E}_{[t]}\}_{t=1}^T$. Here, t indexes a specific event packet in the sequence. Following [29], [37], an event packet, $\mathcal{E}_{[t]}$, is represented as a voxel grid $H \times W \times C$ with each voxel corresponding to a particular spatial and temporal interval. The voxel value will be 1 if the number of events within the voxel is larger than a preset threshold, and 0 otherwise. This representation better preserves the temporal information of events, rather than collapsing them onto a single frame as mentioned in [17]. The processed sequence of event voxel grids is then fed into SNNs as input, denoted as $\mathbf{S}^{\text{in}} \in \{0, 1\}^{T \times H \times W \times C}$.²

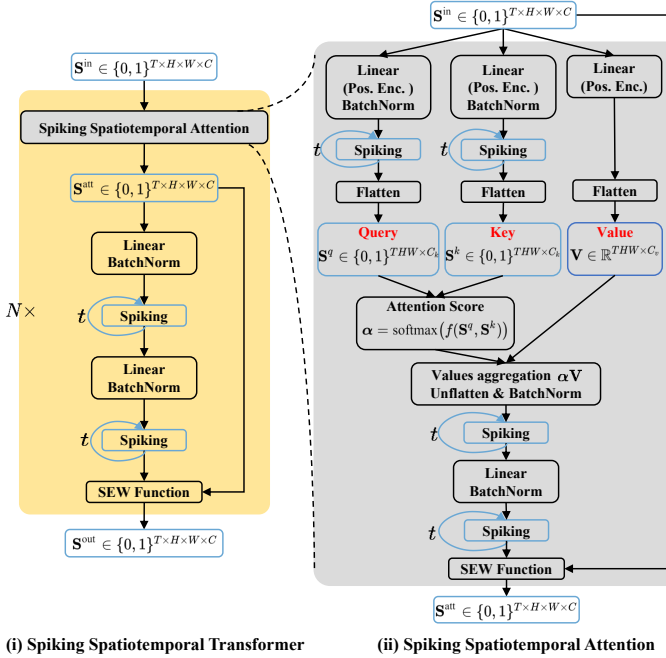
4.2 Spike-Element-Wise Residual Networks

SEW-ResNet, proposed in [24], ranks among the most popular SNNs architectures. Originated from ResNet [31], significant differences are made in the redesign of identity mapping for SNNs using the *SEW Function*, which applies element-wise addition to spike tensors rather than the pre-spiking membrane potentials. This design not only establishes the identity mapping of residual learning in SNNs, but also addresses the vanishing or exploding gradient issue. In our pipeline, it is incorporated as the SNN backbone to extract spike pose features. The spatial size of the output is $1/32$ of the input with a channel size of 512 for SEW-ResNet18, 34 and 2048 for SEW-ResNet50, 101, 152. The detailed architecture of SEW-ResNet is presented in the supplementary material.

4.3 Spiking Spatiotemporal Transformer

Spiking Spatiotemporal Transformer is shown in Fig. 3 (i). Given the input $\mathbf{S}^{\text{in}} \in \{0, 1\}^{T \times H \times W \times C}$, the first step is to apply spiking spatiotemporal attention to combine bidirectional space-time features. A more comprehensive explanation of the attention module will be given later. It is followed by two linear spiking layer with batch normalization, also known as Feed-Forward Network (FFN) in the standard transformer [32]. The final step in the module is

² For clarity, we will generally refer to the size of input spike tensor for different blocks or modules as $T \times H \times W \times C$ in subsequent sections.



(i) Spiking Spatiotemporal Transformer (ii) Spiking Spatiotemporal Attention
 Fig. 3. (a) Architecture of our Spiking Spatiotemporal Transformer that can be stacked by N layers. (b) Architecture of Spiking Spatiotemporal Attention that enables bi-directional flow of information in SNNs, thus facilitate the circulation of pose related information particularly for pose estimation of the early time steps. Normalized Hamming similarity is proposed for the attention score, which is shown as on par to the inner product similarity between real valued vectors, as used in standard transformer.

to apply SEW Function to the output of FFN and input spike tensor for residual learning. Then we get the output $\mathbf{S}^{\text{out}} \in \{0, 1\}^{T \times H \times W \times C}$. This entire module can be stacked by N layers similar to the standard transformer [32].

Spiking Spatiotemporal Attention is illustrated in Fig. 3 (ii). To address the issue of one-directional temporal dependency flow in spiking layers of SNNs, in this module, self-attention is attended in the full space-time domain of spike tensors. Specifically, provided with the input spike tensor $\mathbf{S}^{\text{in}} \in \{0, 1\}^{T \times H \times W \times C}$, to obtain the spike query and key tensors $\mathbf{S}^q, \mathbf{S}^k \in \{0, 1\}^{THW \times C_k}$, we use two linear spiking layers with batch normalization to map the channel size from C to C_k , and then flatten along the spatiotemporal space $T \times H \times W$. Similarly, the real value tensor $\mathbf{V} \in \mathbb{R}^{THW \times C_v}$ is obtained by mapping the channel size to be C_v via a linear layer without spiking and flatten along the spatiotemporal space. Next, the similarity scores between the spiking queries and keys are computed by $f(\mathbf{S}^q, \mathbf{S}^k)$, with its details to be covered later. The softmax function is then applied to obtain the normalized attention weights α for values aggregation, $\alpha \mathbf{V}$. The aggregated value tensor is then unflattened to be $\mathbb{R}^{T \times H \times W \times C_v}$, followed with a batch normalization and spiking layer. Afterwards, we use a spiking linear layer with batch normalization to map the channel size from C_v back to C . Finally, the SEW Function is applied to the attention output and the input spike tensor for residual learning, resulting in the output as $\mathbf{S}^{\text{att}} \in \{0, 1\}^{T \times H \times W \times C}$. It is important to note that our model also supports multi-head attention, following the same procedure used by the standard transformer.

Positional encodings are added in the first layer of the spiking spatiotemporal attention module, aiming to make

the model aware of ordinal information in the input sequence. As the input of the attention module is binary spike tensor while positional encodings are float, direct addition would violate the fast computation in SNNs. So we add the encodings after the linear layer but before the batch normalization and spiking layer. Besides, as the spiking layer generates spikes by rolling over T time steps, we scale the positional encodings by $1/T$ to maintain consistency across models with varying T . The definition mostly follows [32] as

$$\text{PE}(\text{pos}, 2i) = \frac{1}{T} \sin(\text{pos}/10000^{2i/C_k}),$$

$$\text{PE}(\text{pos}, 2i + 1) = \frac{1}{T} \cos(\text{pos}/10000^{2i/C_k}),$$

where pos represents the position in the sequence, while $2i$ or $2i + 1$ denotes the position of C_k channel.

Attention score of scaled dot-product in the standard transformer [32] is not well-defined for the binary spike vectors. Whenever there are zero components in the spike key vector, the dot-product invariably disregards the values of corresponding components in the spike query vector. For instance, assume a spike key vector has its c -th component equal to 0 ($s^k[c] = 0$). Consider two spike query vectors, s_1^q and s_2^q , which differ only in the c -th component, such that $s_1^q[c] = 0$ and $s_2^q[c] = 1$. In this case, the dot-product will always yield the same attention score for the two different queries: $s^{k\top} \cdot s_1^q = s^{k\top} \cdot s_2^q$. That is to say, the dot-product used in [32] is unable to precisely measure the similarity between two binary spike vectors.

Proposition 1 (Johnson–Lindenstrauss Lemma on Binary Embedding [59], [60]). *Let $\mathbf{q}_i, \mathbf{k}_j \in \mathbb{R}^{d_k}$ be a real-valued query and key in the standard transformer described in Sec. 3. Define $s_i^q, s_j^k \in \{0, 1\}^{C_k}$ as the corresponding binary embedding defined as*

$$s_i^q(\mathbf{q}_i) = \text{sign}(\mathbf{A}\mathbf{q}_i), \quad s_j^k(\mathbf{k}_j) = \text{sign}(\mathbf{A}\mathbf{k}_j),$$

where $\mathbf{A} \in \mathbb{R}^{C_k \times d_k}$ is a projection matrix with each entry generated independently from the normal distribution $\mathcal{N}(0, 1)$. Given that $C_k > \frac{\log M}{\delta^2}$ and $\delta > 0$, we have

$$g(d_{\mathcal{H}}(s_i^q, s_j^k) - \delta) \leq d_c(\mathbf{q}_i, \mathbf{k}_j) \leq g(d_{\mathcal{H}}(s_i^q, s_j^k) + \delta), \quad (9)$$

with probability at least $1 - 2e^{-\delta^2 C_k}$. Here $g(x) = \cos(\pi(1-x))$ is a continuous and monotone function for $x \in [0, 1]$ and M is the number of all possible keys and queries given by the finite training set. $d_{\mathcal{H}} \in [0, 1]$ is the normalized Hamming similarity between binary spike vectors defined as

$$d_{\mathcal{H}}(s_i^q, s_j^k) = 1 - \frac{1}{C_k} \sum_{c=1}^{C_k} \mathbb{1}(s_{ic}^q \neq s_{jc}^k), \quad (10)$$

and $d_c \in [0, 1]$ is cosine similarity between real-valued vectors defined as

$$d_c(\mathbf{q}_i, \mathbf{k}_j) = \frac{\mathbf{q}_i^\top \mathbf{k}_j}{\|\mathbf{q}_i\| \|\mathbf{k}_j\|}. \quad (11)$$

Based on Proposition 1, the cosine similarity d_c between real-valued queries and keys is bounded within $[g(d_{\mathcal{H}} - \delta), g(d_{\mathcal{H}} + \delta)]$, where $d_{\mathcal{H}}$ is the normalized Hamming similarity between corresponding binary spike queries and keys. When the channel size C_k is large enough, d_c ensures equivalency to $g(d_{\mathcal{H}})$ with a high probability. The proof is provided in the supplementary. Consequently, as g is a

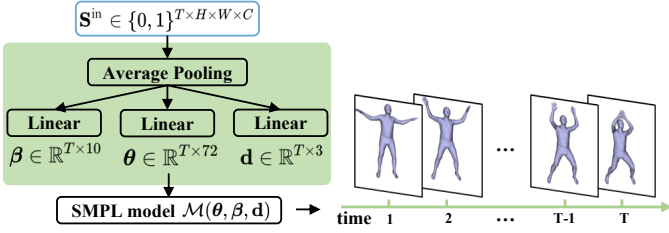


Fig. 4. **Human Poses and Shapes Regression.** The input spike tensor first undergoes 2D average pooling and is then fed into three linear layers in parallel to regress the global translation \mathbf{d} and SMPL pose and shape parameters θ, β across all T time steps.

continuous and monotone for $d_{\mathcal{H}} \in [0, 1]$, we propose to use $d_{\mathcal{H}}$ directly to calculate the attention scores between binary spike queries and keys in our spiking spatiotemporal transformer.

The gradient of normalized Hamming similarity does not exist since Eq. 10 is a non-differentiable function. Thus we approximate $d_{\mathcal{H}}$ by

$$d_{\mathcal{H}}(\mathbf{s}_i^q, \mathbf{s}_j^k) = 1 - \frac{1}{C_k} \sum_{c=1}^{C_k} \left[s_{ic}^q \cdot (1 - s_{jc}^k) + (1 - s_{ic}^q) \cdot s_{jc}^k \right]. \quad (12)$$

As a result, the approximate gradients of normalized Hamming similarity function are given by:

$$\frac{\partial d_{\mathcal{H}}(\mathbf{s}_i^q, \mathbf{s}_j^k)}{\partial s_i^q} = \frac{2s_j^k - 1}{C_k}, \quad \frac{\partial d_{\mathcal{H}}(\mathbf{s}_i^q, \mathbf{s}_j^k)}{\partial s_j^k} = \frac{2s_i^q - 1}{C_k}.$$

4.4 Parametric Pose and Shape Regression

Parametric human pose and shape used in this work is SMPL model [54]. Given the shape parameters β , pose parameters θ and global translations \mathbf{d} , the model outputs a triangular mesh with 6,890 vertices at each time step, that is $\mathcal{M}(\beta, \theta, \mathbf{d}) \in \mathbb{R}^{T \times 6890 \times 3}$ for T time steps in total. The shape parameters at time step t , denoted as $\beta_{[t]} \in \mathbb{R}^{1 \times 10}$, are linear coefficients of PCA shape space, learned from a large number of registered body scans. These parameters mainly describe individual body features such height, weight and body proportions. The pose parameters at time step t , denoted as $\theta_{[t]} \in \mathbb{R}^{1 \times 72}$, represent the articulated poses of the triangular mesh, consisting of a global rotation and relative rotations of the 24 joints in axis-angle form. The global translations of human body at time step t is denoted by $\mathbf{d}_{[t]} \in \mathbb{R}^{1 \times 3}$. To produce the final parametric shapes, the template body is deformed using shape- and pose-dependent deformations, articulated through forward kinematics to its target pose, and further transformed through linear blend skinning and global translation. Meanwhile, the 3D and 2D joint positions, denoted as \mathbf{j}_{3D} and \mathbf{j}_{2D} , are obtained by regressing from the output vertices and projecting the 3D joints onto the 2D images.

We show the process in Fig. 4 where we apply the 2D average pooling to the input spike tensor and then directly regress the shape parameters β , pose parameters θ and global translations \mathbf{d} via three linear layers in parallel. Based on the predicted parameters, we obtain the corresponding parametric shapes and joint positions $\hat{\mathbf{j}}^{3D}, \hat{\mathbf{j}}^{2D}$ by SMPL model across T time steps. When projecting 3D joints on 2D images, as the global translations under the camera coordinate are predicted, we can use predefined camera intrinsic parameters to reduce the redundancy of prediction.

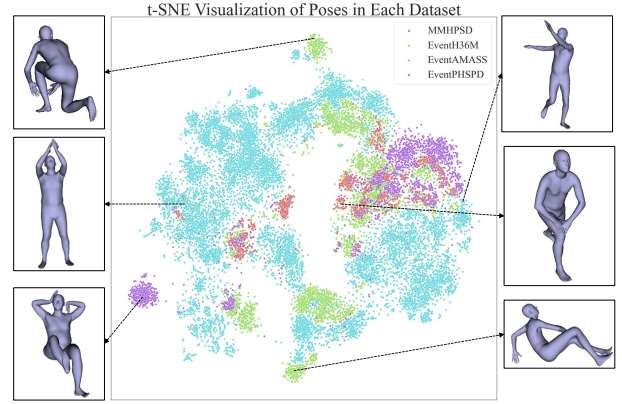


Fig. 5. **t-SNE Visualization of Poses** from each sub-dataset in our SynEventHPD dataset. MMHPSD [38] only covers small areas, while our proposed SynEventHPD, including 4 sub-datasets (EventH36M, EventAMASS, EventPHSPD and SynMMHPSD), span a wide range of pose areas. This highlights the rich variety of poses provided in SynEventHPD, in contrast to the limited range in MMHPSD.

TABLE 1

Summary of event-based datasets for 3D human pose tracking, including existing MMHPSD dataset and 4 sub-datasets in our SynEventHPD dataset, compared in terms of real or synthetic data (R/S), number of subjects (Sub #), number of event streams (Str #), total time length of all the event streams in hours (Len), average time length of each stream in minutes (AvgLen), annotated poses (Pose).

Dataset	R/S	Sub #	Str #	Len (hrs)	AvgLen (mins)	Pose
MMHPSD [29]	Real	15	178	4.39	1.48	✓
EventH36M	Syn	7	835	12.46	0.90	✓
EventAMASS	Syn	13	8028	23.54	0.18	✓
EventPHSPD	Syn	12	156	5.33	2.05	✓
SynMMHPSD	Syn	15	178	4.39	1.48	✓
SynEventHPD (Total)	Syn	47	9197	45.72	0.30	✓

The training losses for our model are introduced as follows:

$$\mathcal{L} = \lambda_{\text{pose}} \mathcal{L}_{\text{pose}} + \lambda_{\text{shape}} \mathcal{L}_{\text{shape}} + \lambda_{\text{trans}} \mathcal{L}_{\text{trans}} + \lambda_{3D} \mathcal{L}_{3D} + \lambda_{2D} \mathcal{L}_{2D},$$

where $\lambda_{\text{pose}}, \lambda_{\text{shape}}, \lambda_{\text{trans}}, \lambda_{3D}$ and λ_{2D} are the corresponding loss weights. We use the losses of pose and shape parameters, global translations 3D and 2D joint positions for training, with the detailed definitions included in the supplementary.

4.5 Our Large-scale Synthetic SynEventHPD Dataset

Currently, the largest event-based dataset for human pose estimation is MMHPSD, which includes 15 subjects, 21 different actions and a total of 4.39 hours of event streams [29]. However, this dataset's limited variety of motions restricts the generalization ability of trained models. To address this issue, we propose to synthesize event data from multiple motion capture datasets, including *i.e.* Human3.6M [51], AMASS [52], PHSPD [53] and MMHPSD-Gray [29], to construct a large-scale synthetic dataset. Our synthetic dataset, called SynEventHPD, is a meta dataset consisting of 4 sub-datasets: EventH36M, EventAMASS, EventPHSPD and SynMMHPSD. In total, it contains 45.72 hours of event streams, which is more than 10 times the size of MMHPSD. The distribution of poses across all these datasets are visualized in Fig. 5 to highlight the variety. Other details are summarized in Table 1. This dataset will be public available for research purpose upon paper acceptance.

The synthesizing process of our new dataset is mainly based on the workflow proposed in [38]. We start by cropping frames according to a global bounding box of person

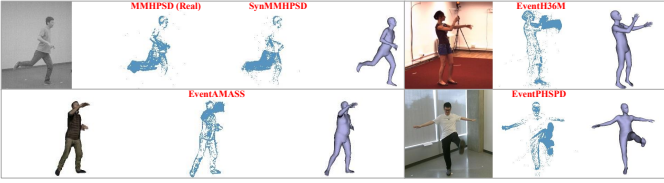


Fig. 6. **Sample examples** of the synthesized event signals from the existing benchmark datasets that are incorporated as sub-datasets in our SynEventHPD dataset. The displayed event image is for visualization purpose, obtained by collapsing events into one frame. Their corresponding RGB or gray-scale images and the annotated poses are also shown. The synthesized event frame from SynMMHPSD is visually indistinguishable from the real events in MMHPSD.

in the video, and then resize to 512×512 to maintain a same image size across different sub-datasets. Next, we apply frame interpolation to increase the frame rate of provided videos, guided by the predicted optical flows. We convert the high frame rate videos to gray-scale images and generate events by checking the brightness change at each pixel over time. This process is straightforward for Human3.6M [51], PHSPD [53] and MMHPSD [29], as they contain RGB or gray-scale videos. However, AMASS [52] dataset only contains motion capture data without any RGB videos. In this regard, for each motion capture sequence, an avatar is randomly picked from 13 different avatars, animated and rendered to form its corresponding RGB videos of size 512×512 , obtained using one of the 4 predefined lightning conditions. Annotations provided in our dataset include pose and shape parameters of SMPL model, corresponding 2D/3D joint positions and the global translation under the default camera intrinsic parameters. We demonstrate the effectiveness of our large-scale synthetic dataset by showing four examples of images, event frames, and annotated poses in Fig. 6. More details and additional examples are included in the supplementary material.

5 EXPERIMENTS

5.1 Empirical Results on MMHPSD Dataset

In this section, we start by outlining the implementation details for training and explaining the reported evaluation metrics. Subsequently, we compare our method with recent video-based and event-based human pose estimation approaches in Sec. 5.1.1, emphasizing the competence of event signals for human pose tracking. We also compare our SNN model with three popular ANN models in Sec. 5.1.2, illustrating the efficiency and effectiveness of our SNN-based approach. Moreover, we contrast our approach with five recently proposed SNN models in Sec. 5.1.3, showcasing the superiority of our proposed Spiking Spatiotemporal Transformer for bi-directional temporal information fusion in human pose tracking.

Implementation Details. For a fair comparison with prior works [28], [29], we follow the train and test set split for the MMHPSD dataset from [29], where subject 1, 2 and 7 are designated for testing and the remaining 12 subjects for training. We present the results of model trained with $T = 8$ time steps and $T = 64$ time steps. For event stream preprocessing, we convert each event packet into a voxel grid of size $256 \times 256 \times 4$. Empirically, we find that $C = 4$ is the best choice, as higher values do not show performance improvements in the ablation study. To fairly compare with other baselines in terms of the number of parameters, we

use SEW-ResNet50 [24] as the backbone and configure the Spiking Spatiotemporal Transformer with 1024 hidden dimension, 1 attention head and 2 layers, resulting in 47.7M parameters.

During training, to ensure robustness against both fast and slow motions, we augment the training samples in two ways: randomly selecting event stream of (0.5, 1, 2, 3) seconds for $T = 8$ and (4, 8, 16, 32) seconds for $T = 64$ as the input, spatially rotating the voxel grid with a random degree between -20 and 20. We use parametric LIF neuron with soft reset and retain the backpropagation of reset path in SNNs, where SpikingJelly [61] is used to implement the model. The loss weights λ_{pose} , λ_{shape} , λ_{trans} , λ_{3D} and λ_{2D} are set to be 10, 1, 50, 1 and 10 respectively. We train the two models for 20 and 25 epochs respectively with batch size being 8. The learning rate starts from 0.01 and is scheduled by CosineAnnealingLR, with maximum epoch number of 21 and 26. The models are trained on a single NVIDIA A100 GPU. For testing, 1 and 8-second event streams are used for $T = 8$ and $T = 64$ models respectively.

Evaluation metrics. Similar to previous works [15], [29], we report three different metrics, mean per joint position error (MPJPE), pelvis-aligned MPJPE (PEL-MPJPE) and Procrustes-Aligned MPJPE (PA-MPJPE). PA-MPJPE compares predicted and target pose after rotation and translation alignment, while PEL-MPJPE compares after only translation alignment of two pelvis joints.

5.1.1 Comparison with Prior Works

We compare our method with four prior works to highlight the competency of using event signals only for human pose tracking: VIBE [15], MPS [55], EventCap [28], and EventHPE [29]. In Tab. 2, we use V , G and E to represent the input data of gray-scale video, first gray-scale image and event streams respectively. $VIBE$ and MPS are applied as the most recent video-based baselines with ResNet50 as the backbone. Note that both methods use weak camera model without global translation, so we will not report their MPJPE. To extract initial poses from the gray-scale video as required by EventCap, we make use of pre-trained VIBE and MPS methods for the extraction, labeled as $EventCap(VIBE)$ and $EventCap(MPS)$. Since the authors have not published their code, we re-implement EventCap using PyTorch LBFGS optimizer and PyTorch3D differential render, following [29]. Besides, EventCap is an iterative optimization approach, which typically requires much more FLOPs than end-to-end methods as is indicated in Tab. 2. For EventHPE, we also use VIBE and MPS for the starting pose extraction, denoted as $EventHPE(VIBE)$ and $EventHPE(MPS)$. We also report the results of EventHPE with ground-truth starting pose known, denoted as $EventHPE(GT)$. This method is considered the upper bound as it is assumed to have perfect information of the starting pose in the first frame, without any pose errors induced by VIBE or MPS.

As shown in Tab. 2, the most recent MPS outperforms VIBE by approximately 9mm in PEL-MPJPE and 5mm in PA-MPJPE for both $T = 8$ and $T = 64$. This trend is also evident when comparing EventCap(MPS) with EventCap(VIBE) or EventHPE(MPS) with EventHPE(VIBE), indicating that the performance of the two prior works [28], [29] is significantly impacted by the accuracy of initial poses provided by the pre-trained video-based methods. When

TABLE 2

Quantitative results of human pose tracking on the MMHPSD test set. Models are trained using the MMHPSD train set for a fair comparison with prior works. The input setting is various, including video (V), first gray-scale frame (G), events (E) and their combination. *VIBE* [15] and *MPS* [55] are video-based ANN methods. *EventCap* [28] and *EventHPE* [29] are most recent works using event camera for human pose tracking. We also include three popular ANN models (*ResNet-GRU* [15], *ResNet-TF* [49] and *Video-Swin* [50]), one mixed model (*SEW-ResNet-TF*) and four SNN models (*ANN2SNN* [39], *SEW-ResNet* [24], *MA-SNN* [46] and *SpikeFormer* [47]) as benchmarks to illustrate the effectiveness of our SNN approach with novel Spiking Spatiotemporal Transformer. Underline denotes the best value except EventHPE(GT). † *EventHPE(GT)* means the ground-truth starting pose is known in EventHPE, which is considered as the upper bound among all these models due to its perfect information of the starting pose in the first frame.

Method	ANN/SNN	Input	Params	T=8 (1 sec)				T=64 (8 secs)			
				FLOPs	MPJPE ↓	PEL-MPJPE ↓	PA-MPJPE ↓	FLOPs	MPJPE ↓	PEL-MPJPE ↓	PA-MPJPE ↓
VIBE [15]	ANN	V	48.3M	43.4G	-	73.1	50.9	344.9G	-	75.4	53.6
MPS [55]		V	39.6M	45.6G	-	68.0	48.2	348.3G	-	69.2	50.1
EventCap(VIBE) [28]	ANN	V+E	48.3M	185.0G	-	71.9	50.4	1477.7G	-	74.1	52.9
EventCap(MPS) [28]		V+E	39.6M	187.2G	-	66.6	47.8	1481.1G	-	68.1	49.5
EventHPE(VIBE) [29]		G+E	49.0M	49.0G	-	69.6	48.9	354.0G	-	71.6	50.2
EventHPE(MPS) [29]		G+E	39.6M	49.3G	-	65.1	46.5	354.2G	-	66.8	48.1
†EventHPE(GT) [29]		G+E	46.9M	-	71.8	55.0	43.9	-	74.5	58.1	45.3
ResNet-GRU [15]	ANN	E	46.9M	43.6G	111.2	60.0	45.3	348.6G	115.0	64.2	49.5
ResNet-TF [49]		E	41.3M	50.5G	108.5	59.9	<u>44.1</u>	403.8G	114.2	66.0	50.1
Video-Swin [50]		E	48.9M	44.7G	124.1	66.5	49.0	359.6G	130.9	72.5	53.1
SEW-ResNet-TF	Mix	E	47.0M	24.5G	110.8	58.9	44.2	199.7G	113.2	65.3	49.3
ANN2SNN [39]	SNN	E	46.9M	12.5G	140.3	74.1	55.8	98.8G	148.2	81.1	60.9
SEW-ResNet [24]		E	<u>25.8M</u>	9.1G	116.8	62.5	48.3	56.7G	122.8	66.3	52.3
MA-SNN [46]		E	30.2M	<u>7.5G</u>	115.2	61.6	47.6	<u>55.3G</u>	120.1	64.8	48.9
SpikeFormer [47]		E	36.8M	13.2G	112.5	60.2	46.8	96.3G	118.1	64.1	48.4
Ours	SNN	E	47.7M	9.4G	<u>107.1</u>	<u>58.8</u>	<u>44.1</u>	63.4G	<u>111.8</u>	<u>61.7</u>	<u>45.6</u>

the initial poses are inaccurate, they might fall into a local minimum and only improve the initial states by up to 3mm in PEL-MPJPE and 2mm in PA-MPJPE. In contrast, our end-to-end approach directly uses event streams, which are better to capture the motion dynamics than images. Consequently, our SNN-based model achieves the best performance with the smallest gap to the upper bound EventHPE(GT) while using only about 6% of FLOPs required by the optimization-based EventCap and 20% of FLOPs needed by the EventHPE. This is further illustrated in Fig. 7, where the inaccurate initial or starting poses given by MPS lead to sub-optimal pose tracking outcomes compared to ours.

5.1.2 Comparison with ANN models

To further illustrate the advantages of SNNs over ANNs in event-based human pose tracking, we compare our model with three popular ANN-based models: ResNet with GRU used in [15], [29] (*ResNet-GRU*), ResNet with standard transformer [32] used in DETR [49] (*ResNet-TF*) and Video Swin Transformer proposed in [50] (*Video-Swin*). For fair comparisons, we select the architecture with about 45M parameters for all the models. Further details are presented in the supplementary material. The settings for training these ANN models mostly follow those of our approach, except the learning rate, which starts from 0.0001 and is scheduled by StepLR with a 0.1 decay after 15 and 20 epochs for both T=8 and T=64, respectively. This is because ANN models do not converge well using a higher learning rate, such as 0.001.

For the models of $T = 8$ in Tab. 2, our approach achieves slightly lower pose errors than ResNet-GRU and Video-Swin, while presenting competitive performance with ResNet-TF, which also achieves 44.1mm in PA-MPJPE.

In the case of $T = 64$, where longer temporal dependencies are necessary for perception, the performance decline of the three ANN-based models is noticeably larger than that of our SNN-based model, with over 4.1mm vs. 1.5mm drop in PA-MPJPE. Furthermore, our model requires only 9.4G and 63.4G FLOPs for $T = 8$ and $T = 64$, respectively, which is less than 20% of the FLOPs needed by the three ANN-based models. These results demonstrate the superiority of our SNN-based approach in efficiently encoding long-term temporal dependencies within event streams, primarily due to the fundamentally different working mechanisms of spiking neurons compared to conventional artificial neurons.

5.1.3 Comparison with SNN models

In Tab. 2, we compare our approach with five recently proposed SNN-based models to highlight the superiority of our proposed Spiking Spatiotemporal Transformer for human pose tracking. *SEW-ResNet-TF* acts as a baseline of mixed architecture that employs SEW-ResNet as the SNN-based backbone followed by an ANN-based standard Transformer for pose tracking. The model architecture settings are similar to our approach. *ANN2SNN* refers to the conversion of the ANNs model of ResNet-GRU to the SNNs model using [39]. *SEW-ResNet* [24] is the backbone used in our approach without Spiking Spatiotemporal Transformer. *MA-SNN* [46] represents multi-dimensional attention SNNs where SEW-ResNet50 is used for a fair comparison. *SpikeFormer* [47] indicates an SNN-based vision transformer (ViT) [62], where dot-product is directly adopted in the self-attention module.

Compared to the mixed model SEW-ResNet-TF, our approach exhibits slightly lower pose errors while requiring less than 50% of FLOPs. As for the entirely SNN-based models, although ANN2SNN has shown its excellent per-

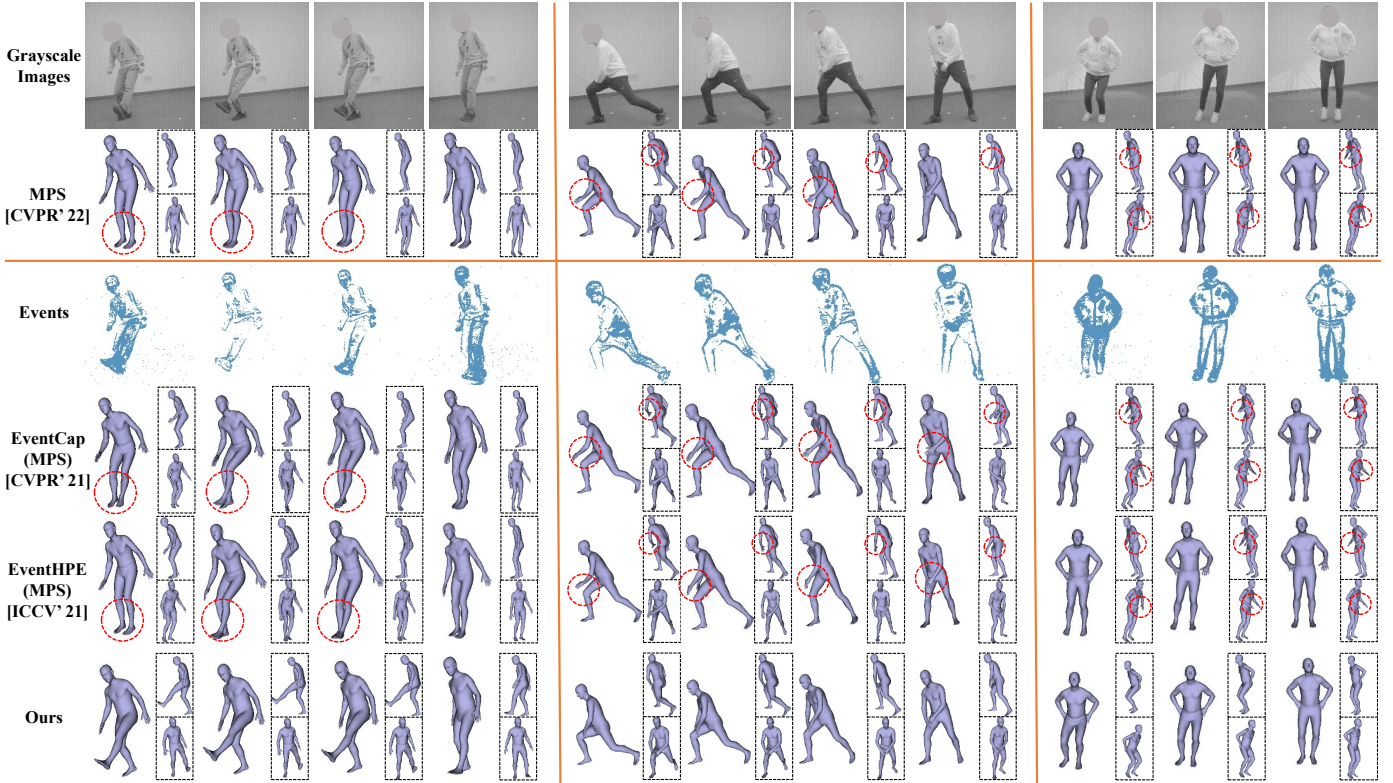


Fig. 7. **Qualitative results** of MPS [55], EventCap(MPS) [28], EventHPE(MPS) [29] and ours. Two side views are shown in dashed boxes. The two prior works, EventCap and EventHPE, tend to suffer from the inaccurate initial poses or starting pose given by pre-trained video based method, MPS, and thus produce sub-optimal pose tracking outcomes when compared to our approach.

formance in the image classification task, it falls short in the regression task of pose tracking, producing much higher pose errors than other directly trained SNNs. This is primarily due to the quantization errors introduced during the conversion process. When compared to SEW-ResNet, our approach yields much lower pose errors – 48.3 vs. 44.1mm in PA-MPJPE for $T = 8$ – and the performance gap widens for $T = 64$, at 52.3 vs. 45.6mm. This demonstrates the importance of bi-directional temporal information provided by our proposed Spiking Spatiotemporal Transformer. In terms of MA-SNN, although it requires fewer FLOPs than our approach due to its lower spiking rate of 16.4% vs. ours of 22.6%, its performance is still inferior. Additionally, our approach presents moderately lower pose errors and fewer FLOPs than SpikeFormer, which is attributed to our proposed normalized Hamming similarity in the spiking attention module, as opposed to the ill-posed dot-product between spike tensors.

5.2 Empirical Results on SynEventHPD Dataset

Although this dataset covers a variety of motions, as illustrated in Fig. 5, the potential domain gap between synthetic and real events data remains an open question. In this section, we aim to demonstrate the value of our proposed synthetic SynEventHPD dataset. We select five models from Tab. 2 including one ANN model (*ResNet-GRU* [15]), one mixed model (*SEW-ResNet-TF*) and three SNN models (*SEW-ResNet* [24], *MA-SNN* [46] and *Ours*). All models are evaluated on the real MMHPSD test set, but are trained using either the real MMHPSD train set, the synthetic SynEventHPD dataset or a combination of both synthetic dataset and the real train set.

TABLE 3
Quantitative results on the real MMHPSD test set. Models are trained using only the real MMHPSD train set (*Real*), only the synthetic SynEventHPD dataset (*Syn*) or a combination of the synthetic SynEventHPD dataset and the real MMHPSD train set (*Syn&Real*). Note that the results of *Real* are the same with those in Tab. 2. The values in the bracket are the improvements of each model trained with *Syn&Real* compared to trained with *Real* only.

Model	ANN/SNN	Training Set	T=8 (1 sec)		
			MPJPE ↓	PEL-MPJPE ↓	PA-MPJPE ↓
ResNet-GRU [15]	ANN	Syn	113.6	62.2	47.5
		Real	111.2	60.0	45.3
		Syn&Real	105.4 (5.8)	58.9 (1.1)	44.6 (0.7)
SEW-ResNet-TF	Mix	Syn	114.1	60.6	45.5
		Real	110.8	58.9	44.2
		Syn&Real	104.2 (6.6)	58.4 (0.5)	43.5 (0.7)
SEW-ResNet [24]		Syn	120.3	63.6	49.1
		Real	116.8	62.5	48.3
		Syn&Real	113.1 (3.7)	61.7 (0.8)	47.8 (0.5)
MA-SNN [46]	SNN	Syn	119.0	63.1	48.8
		Real	115.2	61.6	47.6
		Syn&Real	112.5 (2.7)	60.7 (0.9)	46.9 (0.7)
Ours		Syn	110.7	59.4	45.0
		Real	107.1	58.8	44.1
		Syn&Real	103.1 (4.0)	58.4 (0.4)	43.8 (0.3)

The quantitative results are displayed in Tab. 3. It is evident that, compared to models trained using the real MMHPSD train set, the pose errors are generally higher for models trained on the synthetic SynEventHPD dataset. This is largely due to the domain gap between the synthetic and real events, which results in inferior performance when training only on synthetic data and then evaluating on real data. However, after combining both real and synthetic datasets for training, all the models in Tab. 3 achieve improved performance compared to using either the real



Fig. 8. Generalization ability of our model, trained solely on the synthetic SynEventHPD dataset and applied to unseen scenarios. The left two examples show predicted poses using events synthesized from webcam videos, while the right example employs real events for inference of poses over time.

MMHPSD train set or the synthetic SynEventHPD dataset alone. This highlights the effectiveness of our proposed SynEventHPD dataset. We also present qualitative results in Fig. 8, illustrating the performance of our model trained solely on the synthetic SynEventHPD dataset and applied to unseen scenarios. The left two examples show predictions on synthetic events generated from webcam videos, while the right example displays test results on real data. Despite being trained on the synthetic dataset, our model still demonstrates its generalization ability and applicability.

5.3 Empirical Results on DHP19 Dataset

DHP19 dataset [27] only provides 2-view event streams and annotated 3D joint positions. As a result, we follow the settings in [27], using event streams as input and predicting 2D joint heatmaps as output. Subsequently, 3D pose can be reconstructed using the predicted 2-view 2D poses. We include the quantitative results in the supplementary material, demonstrating the effectiveness and efficiency of SNNs and our proposed Spiking Spatiotemporal Transformer for improved bi-directional temporal information fusion.

5.4 Ablation Study

In this section, we perform ablation studies to assess several crucial components in our model. The quantitative results can be found in the corresponding sub-figures of Fig. 9.

1. Score function in Spiking Spatiotemporal Transformer: We compare our proposed normalized Hamming similarity between spike vectors to scaled dot-production similarity, normalized Euclidean similarity and normalized Manhattan similarity as detailed below:

$$\text{Normalized Hamming similarity} = 1 - \frac{1}{C_k} \sum_{c=1}^{C_k} \mathbb{1}(s_{ic}^q \neq s_{jc}^k),$$

$$\text{Scaled dot-product similarity} = \frac{1}{\sqrt{C_k}} \sum_{c=1}^{C_k} s_{ic}^q \cdot s_{jc}^k,$$

$$\text{Normalized Euclidean similarity} = 1 - \frac{1}{C_k} \sum_{c=1}^{C_k} (s_{ic}^q - s_{jc}^k)^2,$$

$$\text{Normalized Manhattan similarity} = 1 - \frac{1}{C_k} \sum_{c=1}^{C_k} |s_{ic}^q - s_{jc}^k|.$$

The quantitative results of PEL-MPJPE depicted in Fig. 9 (i) reveal that our approach outperforms the other three commonly used similarity functions by over 3mm, showcasing the effectiveness of the normalized Hamming similarity as the score function for spike vectors.

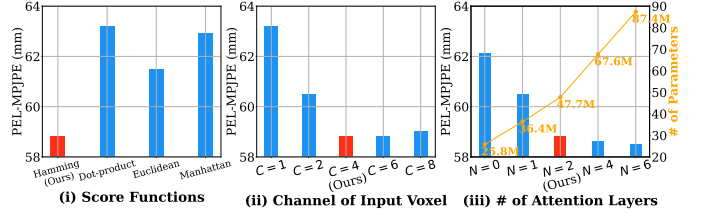


Fig. 9. Ablation studies. (i) Score Functions shows the results of four similarity functions used in the spiking spatiotemporal transformer. (ii) Channel of Input Voxel presents the effects of different channel sizes on the performance of pose tracking. (iii) # of Attention Layers investigates the performance with different number of attention layers in the spiking spatiotemporal transformer.

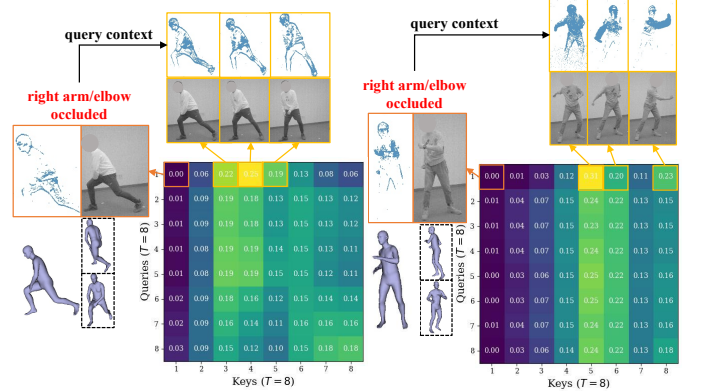


Fig. 10. Visualization of attention score maps. Our approach determines accurate poses for obscured body parts at an early stage using spiking spatiotemporal attention, in which the query at $t = 1$ places significantly greater emphasis on features from later time steps.

2. Channel C of input voxel: We compare channel sizes of 1, 2, 4, 6 and 8 in terms of PEL-MPJPE in Fig. 9 (ii). The results show that $C=4$ yields lower joint errors compared to sizes of 1 and 2, while nearly the same errors as sizes 6 and 8. Therefore, $C=4$ is empirically determined to be the appropriate choice for the channel size.

3. # of attention layers: We compare our model with 0, 1, 2, 4 and 6 layers in Spiking Spatiotemporal Transformer in Fig. 9 (iii). The improvement of PEL-MPJPE is noticeable when using 1 or 2 layers of attention in our spiking transformer. However, this improvement is minimal for 4 and 6 layers, accompanied by a dramatic increase in the number of parameters from 47.7M to 87.4M.

5.5 Discussion

Attention scores maps are shown in Fig. 10. For better visualization, we transform the attention score matrix from $THW \times THW$ to $T \times T$, where the attention weights of spatial positions at each time step are summed together. The two examples illustrate that our attention mechanism allows the query at $t = 1$ to focus predominantly on features originating from subsequent time steps, thereby providing a more accurate and efficient prediction of body part positions even when they are obscured. The success of these examples can be attributed to its ability to globally adapt to the temporal dependencies present in the input event stream. By emphasizing the relevant features from temporal context, our method can effectively compensate for the lack of information due to occlusion in the initial stages. This results in more accurate and robust pose tracking through time from events only.

Failure cases are displayed in Fig. 11, where the pose are not accurately estimated from the events. These cases

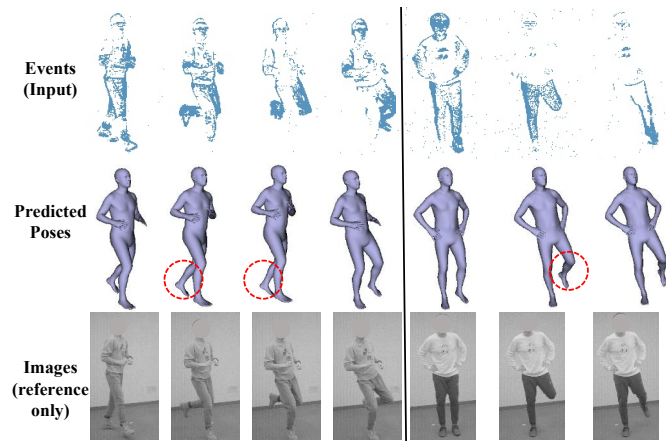


Fig. 11. **Failure cases.** Owing to the presence of body part occlusion and also the absence of temporal context, our method struggles to accurately estimate poses, as indicated by the red circles.

were primarily attributed to the presence of body part occlusion and the absence of temporal context. The impact of occlusion can be significant, as it hinders the model’s ability to detect and analyze essential features required for pose estimation. Moreover, unlike the examples in Fig. 10, the lack of temporal context further compounds this issue, as the model cannot effectively leverage information from previous or subsequent frames to compensate for missing or obscured data. Recognizing and addressing these failure cases is crucial for improving the robustness and reliability of our event-based pose tracking method.

6 CONCLUSION AND OUTLOOK

We present in this paper a dedicated end-to-end SNN-based approach for event-based pose tracking, where events are the only source of input, thus removing the need of additional RGB or gray-scale images. Our approach is based entirely upon SNNs and our proposed Spatiotemporal Transformer demonstrates its effectiveness for bi-directional temporal feature compensation. A large-scale synthetic dataset is also constructed, featuring a broad and diverse set of annotated 3D human motions, as well as longer hours of event stream data. Empirical experiments demonstrate the superiority of our approach in both efficacy and efficiency measures.

For future work, we plan to extend our dataset to incorporate multi-view event streams, as well as the presence and interaction of multiple human characters. They pose new challenges on the development of our SNN-based approach to address multi-view and multi-person scenarios.

REFERENCES

- [1] J. Shotton, R. Girshick, A. Fitzgibbon, T. Sharp, M. Cook, M. Finocchio, R. Moore, P. Kohli, A. Criminisi, A. Kipman *et al.*, “Efficient human pose estimation from single depth images,” *IEEE TPAMI*, vol. 35, no. 12, pp. 2821–2840, 2012.
- [2] R. Zhao, Y. Wang, and A. M. Martinez, “A simple, fast and highly-accurate algorithm to recover 3d shape from 2d landmarks on a single image,” *IEEE TPAMI*, vol. 40, no. 12, pp. 3059–3066, 2017.
- [3] K. Wang, L. Lin, C. Jiang, C. Qian, and P. Wei, “3d human pose machines with self-supervised learning,” *IEEE TPAMI*, vol. 42, no. 5, pp. 1069–1082, 2020.
- [4] C. Xu, L. N. Govindarajan, Y. Zhang, and L. Cheng, “Lie-x: Depth image based articulated object pose estimation, tracking, and action recognition on lie groups,” *IJCV*, vol. 123, no. 3, pp. 454–478, 2017.
- [5] C. Wang, Y. Wang, Z. Lin, A. L. Yuille, and W. Gao, “Robust estimation of 3d human poses from a single image,” in *CVPR*, 2014, pp. 2361–2368.
- [6] X. Zhou, M. Zhu, S. Leonardos, K. G. Derpanis, and K. Daniilidis, “Sparseness meets deepness: 3d human pose estimation from monocular video,” in *CVPR*, 2016, pp. 4966–4975.
- [7] S. Park, J. Hwang, and N. Kwak, “3d human pose estimation using convolutional neural networks with 2d pose information,” in *ECCV*. Springer, 2016, pp. 156–169.
- [8] S. Li, W. Zhang, and A. B. Chan, “Maximum-margin structured learning with deep networks for 3d human pose estimation,” in *ICCV*, 2015, pp. 2848–2856.
- [9] A. Kanazawa, M. J. Black, D. W. Jacobs, and J. Malik, “End-to-end recovery of human shape and pose,” in *CVPR*, 2018.
- [10] G. Pavlakos, L. Zhu, X. Zhou, and K. Daniilidis, “Learning to estimate 3d human pose and shape from a single color image,” in *CVPR*, 2018, pp. 459–468.
- [11] Y. Xu, S.-C. Zhu, and T. Tung, “Denserac: Joint 3d pose and shape estimation by dense render-and-compare,” in *CVPR*, 2019, pp. 7760–7770.
- [12] N. Kolotouros, G. Pavlakos, M. J. Black, and K. Daniilidis, “Learning to reconstruct 3d human pose and shape via model-fitting in the loop,” in *ICCV*, 2019, pp. 2252–2261.
- [13] K. Lin, L. Wang, and Z. Liu, “End-to-end human pose and mesh reconstruction with transformers,” in *CVPR*, 2021, pp. 1954–1963.
- [14] A. Kanazawa, J. Y. Zhang, P. Felsen, and J. Malik, “Learning 3d human dynamics from video,” in *CVPR*, 2019, pp. 5614–5623.
- [15] M. Kocabas, N. Athanasiou, and M. J. Black, “Vibe: Video inference for human body pose and shape estimation,” in *CVPR*, June 2020, pp. 5253–5263.
- [16] Y. Yuan, U. Iqbal, P. Molchanov, K. Kitani, and J. Kautz, “Glamr: Global occlusion-aware human mesh recovery with dynamic cameras,” in *CVPR*, 2022, pp. 11 038–11 049.
- [17] G. Gallego, T. Delbruck, G. Orchard, C. Bartolozzi, B. Taba, A. Censi, S. Leutenegger, A. Davison, J. Conradt, K. Daniilidis, and D. Scaramuzza, “Event-based vision: A survey,” *IEEE TPAMI*, vol. 44, no. 1, pp. 154–180, 2022.
- [18] D. Gehrig, H. Rebecq, G. Gallego, and D. Scaramuzza, “Asynchronous, photometric feature tracking using events and frames,” in *ECCV*, 2018, pp. 750–765.
- [19] A. Mitrokhin, C. Fermüller, C. Parameshwara, and Y. Aloimonos, “Event-based moving object detection and tracking,” in *IROS*. IEEE, 2018, pp. 6895–6902.
- [20] J. Zhang, X. Yang, Y. Fu, X. Wei, B. Yin, and B. Dong, “Object tracking by jointly exploiting frame and event domain,” in *ICCV*, 2021, pp. 13 043–13 052.
- [21] J. Zhang, B. Dong, H. Zhang, J. Ding, F. Heide, B. Yin, and X. Yang, “Spiking transformers for event-based single object tracking,” in *CVPR*, 2022, pp. 8801–8810.
- [22] A. Amir, B. Taba, D. Berg, T. Melano, J. McKinstry, C. Di Nolfo, T. Nayak, A. Andreopoulos, G. Garreau, M. Mendoza *et al.*, “A low power, fully event-based gesture recognition system,” in *CVPR*, 2017, pp. 7243–7252.
- [23] J. Kim, I. Hwang, and Y. M. Kim, “Ev-tta: Test-time adaptation for event-based object recognition,” in *CVPR*, 2022, pp. 17745–17754.
- [24] W. Fang, Z. Yu, Y. Chen, T. Huang, T. Masquelier, and Y. Tian, “Deep residual learning in spiking neural networks,” *NeurIPS*, vol. 34, pp. 21 056–21 069, 2021.
- [25] H. Rebecq, G. Gallego, E. Mueggler, and D. Scaramuzza, “Emvs: Event-based multi-view stereo—3d reconstruction with an event camera in real-time,” *IJCV*, vol. 126, no. 12, pp. 1394–1414, 2018.
- [26] K. Zhang, K. Che, J. Zhang, J. Cheng, Z. Zhang, Q. Guo, and L. Leng, “Discrete time convolution for fast event-based stereo,” in *CVPR*, 2022, pp. 8676–8686.
- [27] E. Calabrese, G. Taverni, C. Awai Easthope, S. Skriabine, F. Corradi, L. Longinotti, K. Eng, and T. Delbruck, “Dhp19: Dynamic vision sensor 3d human pose dataset,” in *CVPR Workshop*, 2019.
- [28] L. Xu, W. Xu, V. Golyanik, M. Habermann, L. Fang, and C. Theobalt, “Eventcap: Monocular 3d capture of high-speed human motions using an event camera,” in *CVPR*, 2020, pp. 4968–4978.
- [29] S. Zou, C. Guo, X. Zuo, S. Wang, P. Wang, X. Hu, S. Chen, M. Gong, and L. Cheng, “Eventhpe: Event-based 3d human pose and shape estimation,” in *ICCV*, 2021, pp. 10996–11005.
- [30] V. Rudnev, V. Golyanik, J. Wang, H.-P. Seidel, F. Mueller, M. Elgharib, and C. Theobalt, “Eventhands: real-time neural 3d hand

- pose estimation from an event stream," in *ICCV*, 2021, pp. 12 385–12 395.
- [31] K. He, X. Zhang, S. Ren, and J. Sun, "Deep residual learning for image recognition," in *CVPR*, 2016, pp. 770–778.
- [32] A. Vaswani, N. Shazeer, N. Parmar, J. Uszkoreit, L. Jones, A. N. Gomez, Ł. Kaiser, and I. Polosukhin, "Attention is all you need," *NeurIPS*, vol. 31, 2017.
- [33] A. Zhu, L. Yuan, K. Chaney, and K. Daniilidis, "Ev-flownet: Self-supervised optical flow estimation for event-based cameras," in *RSS*, 2018.
- [34] L. Wang, T.-K. Kim, and K.-J. Yoon, "Eventsr: From asynchronous events to image reconstruction, restoration, and super-resolution via end-to-end adversarial learning," in *CVPR*, 2020, pp. 8315–8325.
- [35] W. Fang, Z. Yu, Y. Chen, T. Masquelier, T. Huang, and Y. Tian, "Incorporating learnable membrane time constant to enhance learning of spiking neural networks," in *ICCV*, 2021, pp. 2661–2671.
- [36] Z. Sun, N. Messikommer, D. Gehrig, and D. Scaramuzza, "Ess: Learning event-based semantic segmentation from still images," in *ECCV*. Springer, 2022, pp. 341–357.
- [37] D. Gehrig, A. Loquercio, K. G. Derpanis, and D. Scaramuzza, "End-to-end learning of representations for asynchronous event-based data," in *ICCV*, 2019, pp. 5633–5643.
- [38] D. Gehrig, M. Gehrig, J. Hidalgo-Carri6, and D. Scaramuzza, "Video to events: Recycling video datasets for event cameras," in *CVPR*, 2020, pp. 3586–3595.
- [39] B. Rueckauer, I.-A. Lungu, Y. Hu, M. Pfeiffer, and S.-C. Liu, "Conversion of continuous-valued deep networks to efficient event-driven networks for image classification," *Frontiers in neuroscience*, vol. 11, p. 682, 2017.
- [40] B. Han, G. Srinivasan, and K. Roy, "Rmp-snn: Residual membrane potential neuron for enabling deeper high-accuracy and low-latency spiking neural network," in *CVPR*, 2020, pp. 13 558–13 567.
- [41] Y. Li, S. Deng, X. Dong, R. Gong, and S. Gu, "A free lunch from ann: Towards efficient, accurate spiking neural networks calibration," in *ICML*, 2021, pp. 6316–6325.
- [42] Z. Yan, J. Zhou, and W.-F. Wong, "Near lossless transfer learning for spiking neural networks," in *AAAI*, vol. 35, no. 12, 2021, pp. 10 577–10 584.
- [43] S. Deng and S. Gu, "Optimal conversion of conventional artificial neural networks to spiking neural networks," in *ICLR*, 2021.
- [44] Y. Li, Y. Guo, S. Zhang, S. Deng, Y. Hai, and S. Gu, "Differentiable spike: Rethinking gradient-descent for training spiking neural networks," *NeurIPS*, vol. 34, pp. 23 426–23 439, 2021.
- [45] X. Yao, F. Li, Z. Mo, and J. Cheng, "Glif: A unified gated leaky integrate-and-fire neuron for spiking neural networks," in *NeurIPS*, 2022.
- [46] M. Yao, G. Zhao, H. Zhang, Y. Hu, L. Deng, Y. Tian, B. Xu, and G. Li, "Attention spiking neural networks," *IEEE TPAMI*, 2023.
- [47] Z. Zhou, Y. Zhu, C. He, Y. Wang, S. Yan, Y. Tian, and L. Yuan, "Spikformer: When spiking neural network meets transformer," in *ICLR*, 2022.
- [48] M. Yao, H. Gao, G. Zhao, D. Wang, Y. Lin, Z. Yang, and G. Li, "Temporal-wise attention spiking neural networks for event streams classification," in *ICCV*, 2021, pp. 10 221–10 230.
- [49] N. Carion, F. Massa, G. Synnaeve, N. Usunier, A. Kirillov, and S. Zagoruyko, "End-to-end object detection with transformers," in *ECCV*. Springer, 2020, pp. 213–229.
- [50] Z. Liu, Y. Lin, Y. Cao, H. Hu, Y. Wei, Z. Zhang, S. Lin, and B. Guo, "Swin transformer: Hierarchical vision transformer using shifted windows," in *ICCV*, 2021, pp. 10 012–10 022.
- [51] C. Ionescu, D. Papava, V. Olaru, and C. Sminchisescu, "Human3.6m: Large scale datasets and predictive methods for 3d human sensing in natural environments," *IEEE TPAMI*, vol. 36, no. 7, pp. 1325–1339, 2013.
- [52] N. Mahmood, N. Ghorbani, N. F. Troje, G. Pons-Moll, and M. J. Black, "Amass: Archive of motion capture as surface shapes," in *ICCV*, 2019, pp. 5442–5451.
- [53] S. Zou, X. Zuo, S. Wang, Y. Qian, C. Guo, and L. Cheng, "Human pose and shape estimation from single polarization images," *IEEE TMM*, 2022.
- [54] M. Loper, N. Mahmood, J. Romero, G. Pons-Moll, and M. J. Black, "Smpl: A skinned multi-person linear model," *ACM TOG*, vol. 34, no. 6, pp. 1–16, 2015.
- [55] W.-L. Wei, J.-C. Lin, T.-L. Liu, and H.-Y. M. Liao, "Capturing humans in motion: temporal-attentive 3d human pose and shape estimation from monocular video," in *CVPR*, 2022, pp. 13 211–13 220.
- [56] J. Deng, W. Dong, R. Socher, L.-J. Li, K. Li, and L. Fei-Fei, "Imagenet: A large-scale hierarchical image database," in *CVPR*. IEEE, 2009, pp. 248–255.
- [57] J. Hagenaaars, F. Paredes-Vallés, and G. De Croon, "Self-supervised learning of event-based optical flow with spiking neural networks," *NeurIPS*, vol. 34, pp. 7167–7179, 2021.
- [58] J. Zhang, L. Tang, Z. Yu, J. Lu, and T. Huang, "Spike transformer: Monocular depth estimation for spiking camera," in *ECCV*. Springer, 2022, pp. 34–52.
- [59] L. Jacques, J. N. Laska, P. T. Boufounos, and R. G. Baraniuk, "Robust 1-bit compressive sensing via binary stable embeddings of sparse vectors," *IEEE Transactions on Information Theory*, vol. 59, no. 4, pp. 2082–2102, 2013.
- [60] X. Yi, C. Caramanis, and E. Price, "Binary embedding: Fundamental limits and fast algorithm," in *ICML*, 2015, pp. 2162–2170.
- [61] W. Fang, Y. Chen, J. Ding, D. Chen, Z. Yu, H. Zhou, Y. Tian, and other contributors, "Spikingjelly," <https://github.com/fangwei123456/spikingjelly>, 2020, accessed: 2023-02-28.
- [62] A. Dosovitskiy, L. Beyer, A. Kolesnikov, D. Weissenborn, X. Zhai, T. Unterthiner, M. Dehghani, M. Minderer, G. Heigold, S. Gelly *et al.*, "An image is worth 16x16 words: Transformers for image recognition at scale," in *ICLR*, 2020.